Am J Cancer Res 2022;12(5):2068-2083
www.ajcr.us /ISSN:2156-6976/ajcr0142347

Original Article

Label-free optical redox ratio from urinary extracellular vesicles as a screening biomarker for bladder cancer

Jaena Park[1,2], Rebecca L Kamerer[3], Marina Marjanovic[1,2,4], Janet E Sorrells[1,2], Sixian You[1,2], Ronit Barkalifa[2], Kimberly A Selting[3], Stephen A Boppart[1,2,4,5,6]

[1]Department of Bioengineering, University of Illinois at Urbana-Champaign, IL, USA; [2]Beckman Institute for Advanced Science and Technology, University of Illinois at Urbana-Champaign, IL, USA; [3]Department of Veterinary Clinical Medicine, University of Illinois at Urbana-Champaign, IL, USA; [4]Carle Illinois College of Medicine, University of Illinois at Urbana-Champaign, IL, USA; [5]Department of Electrical and Computer Engineering, University of Illinois at Urbana-Champaign, IL, USA; [6]Cancer Center at Illinois, University of Illinois at Urbana-Champaign, IL, USA

Received February 14, 2022; Accepted March 30, 2022; Epub May 15, 2022; Published May 30, 2022

Abstract: Extracellular vesicles (EVs) have been studied for their potential applications in cancer screening, diagnosis, and treatment monitoring. Most studies have focused on the bulk content of EVs; however, it is also informative to investigate their metabolic status, and changes under different physiological and environmental conditions. In this study, noninvasive, multimodal, label-free nonlinear optical microscopy was used to evaluate the optical redox ratio of large EVs (microvesicles) isolated from the urine of 11 dogs in three cohorts (4 healthy, 4 transitional cell carcinoma (TCC) of the bladder, and 3 prostate cancer). The optical redox ratio is a common metric comparing the autofluorescence intensities of metabolic cofactors FAD and NAD(P)H to characterize the metabolic profile of cells and tissues, and has recently been applied to EVs. The optical redox ratio revealed that dogs with TCC of the bladder had a more than 2-fold increase in NAD(P)H-rich urinary EVs (uEVs) when compared to healthy dogs, whereas dogs with prostate cancer had no significant difference. The optical redox ratio values of uEVs kept at -20°C for 48 hours were significantly different from those of freshly isolated uEVs, indicating that this parameter is more reliable when assessing freshly isolated uEVs. These results suggest that the label-free optical redox ratio of uEVs, indicating relative rates of glycolysis and oxidative phosphorylation of parent cells and tissues, may act as a potential screening biomarker for bladder cancer.

Keywords: Extracellular vesicle, urine, label-free detection, optical redox ratio, dog, bladder cancer, urogenital cancer, storage, cancer screening

Introduction

Bladder cancer is the 12th most common cancer in humans in the United States, and about 81,180 new cases and 17,100 deaths are expected in 2022. The 5-year relative survival rate is significantly higher when bladder cancer is diagnosed at an earlier stage (70% for localized bladder cancer), whereas the 5-year survival rate for those diagnosed with distant/metastatic bladder cancer is only 6% [1]. Currently, the preferred method for diagnosing bladder cancer is cystoscopy, which has a sensitivity range of 62 to 84% and specificity range of 43 to 98% [2]. However, this method is highly invasive, and has difficulty in detecting small flat lesions and carcinoma *in situ*, resulting in a high recurrence rate of around 50% due to difficulty in tumor localization [3, 4]. Cytology of voided urine is also used to diagnose advanced bladder cancer. However, it lacks the sensitivity to detect it in its early stages, with a sensitivity range of only 4 to 31% [3, 5]. Since urine can be collected repeatedly and noninvasively, there is a strong interest in using this biofluid as a liquid biopsy source for screening, detecting, and monitoring the progression or regression of bladder cancers [3, 6]. Thus, a new, accurate, and sensitive urine screening method that could identify the presence of bladder cancer, and even various stages, would be of great clinical significance.

Extracellular vesicles (EVs) are membrane-encapsulated particles released by various cell types into the extracellular space. Released EVs circulate throughout the body and deliver signals to target cells for inter-cellular communication [7]. EV content is highly heterogeneous and can contain proteins, nucleic acids, and metabolites from their parent cells. Since the EV cargo originates from the parent cells, and since EVs are abundantly found in all bodily fluids, including urine, they have been increasingly investigated for carrying potential diagnostic or prognostic information about the health status or health outcome of the individual.

Characterizing the protein and genetic material in EVs originating from the genitourinary tract (kidney, bladder, prostate) has been shown to reflect various genitourinary diseases, such as bladder cancer and kidney dysfunction [6, 8, 9]. Similarly, EVs originating from urine have also been shown to reflect various dieseases, such as bladder cancer and neurological diseases [3, 10-13]. Small EVs (~30-100 nm), also known as exosomes, have primarily been studied for their potential use as cancer biomarkers because of their increased release from tumor cells [14-17]. Large EVs (~0.1-2 μm), also known as microvesicles, have been given less attention compared to small EVs and thus warrant further investigation. Although small EVs or exosomes originate from the exocytosis of multivesicular bodies and large EVs or microvesicles are released directly from the plasma membrane of the parent cell, both types of EVs are packaged and contain cargo that reflects the content and state of the original parent cell [18, 19].

Various-omics such as transcriptomics, proteomics, and lipidomics have been used with EVs to find biomarkers for various cancers [20-24]. However, many biomarkers discovered by these methods require lysing and labeling techniques, which restrict the re-use of EVs for further analysis or for potential treatment purposes. These analysis methods are also prone to false positive or confounding signals due to the introduced tags [25]. Therefore, label-free techniques that offer the potential for retrieving direct information from the EVs in a non-destructive manner while maintaining their properties for future analysis by other methods are desired.

While EV analysis has traditionally included finding molecular profiles and detecting specific proteins, lipids, and nucleic acids within EVs, or characterizing surface membrane markers on the EVs, only a few studies have focused on the metabolites inside EVs [8-11, 14-19, 26-29]. Both small EVs and large EVs are known to contain flavin adenine dinucleotide (FAD), reduced nicotinamide adenine dinucleotide (NADH), and reduced nicotinamide adenine dinucleotide phosphate (NADPH), which reflect the oxidative state, and thus the metabolic state, of both the EV and the parent cell. In tumors, densely packed cancer cells adapt to hypoxic conditions by altering their aerobic and anaerobic metabolic pathways. These metabolic changes are thus reflected in the concentration of electron transporters (NAD(P)H and FAD), which could be used as an indicator of cancer with its elevated metabolic state [29-33].

Imaging and characterizing EVs can directly provide their physical and optical properties at the single EV level, whereas most EV content analysis methods cannot resolve single EVs and instead report on the average content of a large population [26, 34]. Single EV specificity is especially useful since EV populations are typically highly heterogeneous. Laser trapping enables the accurate imaging and characterization of single EVs [26]. However, the throughput is low. Therefore, imaging multiple EVs at the single EV level is preferred, and more practical. In addition, imaging can provide *in situ* spatial information when performed on tissue specimens or even *in vivo*. However, because of the small size of EVs, only a few imaging studies with fluorescent labeling have been performed [35]. For imaging EVs *in situ* in a fresh resected specimen or an *in vivo* tissue, a non-invasive label-free imaging method is required to interrogate the intact tissue without disturbing it. Transmission electron microscopy (TEM) and scanning electron microscopy (SEM) have been routinely used to image EVs with high resolution without labeling, but these images lack biochemical information and are destructive to the tissue [36, 37]. As an alternative to label-free imaging, fluorescence imaging and bioluminescence imaging require the use of labels or dyes to tag the EVs [38, 39], but these perturbative methods are not highly amenable to detecting and imaging EVs in fresh

cell, tissue, or liquid biopsy specimens, nor *in vivo*.

Simultaneous label-free auto-fluorescence multi-harmonic (SLAM) microscopy was shown to successfully visualize and quantify unlabeled singular EVs, both *in vivo* and in *ex vivo* tissue specimens with high spatial resolution (< 500 nm) [29, 34, 40]. SLAM microscopy incorporates 4 nonlinear optial imaging modalities: second (SHG) and third (THG) harmonic generation, and two-photon (2PF) and three-photon (3PF) excited autofluorescence imaging. Specifically for imaging EVs, the THG channel detects the water-lipid interfaces, providing the morphology and locational information of EVs, and the 2PF and 3PF channels detect the endogenous EV-associated autofluorescence of FAD and NAD(P)H, respectively. Furthermore, the optical redox ratio (ORR, Equation (2)), which is the ratio between the FAD and NAD(P)H autofluorescence intensities, can be determined using the 2PF and 3PF signal channels, and can even be determined for single EVs [29, 33, 41]. The ORR is therefore sensitive to the cellular metabolic activity, such as glycolysis and oxidative phosphorylation, reflected in both the EVs and their parent cells [41, 42].

Optical characteristics of EVs, such as their fluorescence intensity and lifetime of NAD(P)H, and their fluorescence intensity of FAD, have been measured in breast cancer cell lines and breast cancer tissues [27, 29, 34, 40, 43, 44]. For example, NAD(P)H and FAD fluorescence intensities of breast cancer cell- and tissue-derived EVs have been used to distinguish the presence or absence of breast cancer, as well as the aggressiveness of the disease [29]. Fluorescence lifetime of NAD(P)H in breast cancer cell-derived EVs showed that EVs exhibit a wider range of metabolic profiles than their parent cells [34]. Coherent anti-Stokes Raman scattering imaging provided evidence that the biochemical makeup of individual and populations of EVs is associated with their spatial distribution inside breast cancer tissue [44]. These studies showed the potential of using label-free optical imaging of EVs as a platform for cancer screening and detection. However, previous studies focused on imaging EVs inside tissue with SLAM microscopy and required excision of tissue before imaging. Advancing this technology for use with liquid biopsy specimens, such as for urinary EVs (uEVs), has the advantage of being patient-friendly and non-invasive, and shifting the application of this novel technology from being a diagnostic modality to being a screening modality. Imaging and characterizing uEVs from urine samples would also avoid two of the primary constraints of optical imaging, those being limited imaging depth penetration and limited acquisition time.

Client-owned canines were investigated in this feasibility study to explore the concept of using label-free SLAM imaging and characterization of uEVs for bladder cancer screening. Canines are a suitable model because the volume of urine produced is sufficient for isolation of EVs, and naturally occurring bladder and prostate cancer cases in canines are representative cancer models that can be related to humans [45-47]. Also, dogs are the only other large mammal that frequently develops prostate cancer, and have been used regularly for pre-clinical studies [46]. Transitional cell carcinoma (TCC), which develops from urothelial cells inside the bladder, is the most common type of bladder cancer in both humans and dogs, comprising about 90% of bladder cancer cases [47]. Muscle-invasive TCCs are the most common type of TCC in dogs while one-quarter of human TCCs are muscle-invasive [47]. TCC in humans and dogs is comparable in terms of risk factors, histology, mutation profiles, clinical presentation, and metastatic sites [47-49]. Therefore, urine from healthy, TCC-bearing, and prostate cancer-bearing dogs was examined in this study.

In this feasibility study, SLAM microscopy was used to image and analyze the physical and optical properties of uEVs from canines to assess whether the measured ORR could be used as a screening biomarker of genitourinary cancer. Related to the collection, handling, and storage of uEVs, we also evaluated the impact of the analyte storage conditions on the repeatability and reliability of the ORR measurements by SLAM. This represents the first study to characterize uEVs from dogs using label-free nonlinear optical microscopy.

Materials and methods

Dog urine collection

Voided urine samples (ranging from 15 to 180 mL) were collected from 11 client-owned

Table 1. Canine patient demographics. MC: Male castrated, FS: female spayed

Diagnosis	Age (years)	Sex	Species
Transitional cell carcinoma of the bladder	10	FS	Miniature Pinscher
Transitional cell carcinoma of the bladder	7	FS	Airedale Terrier
Transitional cell carcinoma of the bladder	11	FS	Mixed breed
Transitional cell carcinoma of the bladder	11	MC	Scottish Terrier
Prostate carcinoma	8	MC	Mixed breed
Prostate carcinoma	9	MC	Labrador Retriever
Prostate carcinoma	8	MC	Mixed breed
Healthy control	4	MC	Mixed breed
Healthy control	4	FS	Mixed breed
Healthy control	3	FS	Golden Retriever
Healthy control	5	FS	Mixed breed

dogs according to a study protocol approved by the Institutional Animal Care and Use Committee at the University of Illinois at Urbana-Champaign. Prior to enrollment in the study, informed owner consent was obtained. Four dogs with TCC of the bladder and three dogs with prostate carcinoma comprised the genitourinary cancer group (**Table 1**). Four healthy dogs without any symptoms of disease comprised a control group. Dogs were determined to be healthy based on a lack of abnormal health history and physical and chemical examination findings, including urine dipstick testing (Clinitek Status, Siemens, Germany). Urinalysis confirmed that all of the healthy dogs had negative blood, leukocyte, and nitrite levels.

Urinary EV (uEV) isolation

Urinary EVs were isolated using a differential velocity centrifugation method with increasing relative centrifugation force (*g*) following a previously published method (**Figure 1**) [50]. Urine was diluted with PBS to a total volume of 50 mL and was centrifuged in Protein LoBind tubes (Eppendorf, USA) at 800 × *g* (Universal 320 R, Hettich, Germany) for 10 minutes at 4°C. The supernatant was then centrifuged at 2,000 × *g* for 30 minutes at 4°C and the pellet was re-suspended in 100 µL of PBS (**Figure 1**, Fraction 1). Supernatant was collected in polyallomer (PA) thin-wall tubes (Thermo Scientific, USA) and centrifuged at 12,000 × *g* (Sorvall WX+ Ultracentrifuge Series, ThermoFisher, USA) for 1 hour at 4°C. Pellets were re-suspended in 100 µL of PBS (**Figure 1**, Fraction 2), while the supernatant was collected in PA thin-wall tubes and centrifuged at 120,000 × *g* for 80 min at 4°C. Supernatant was removed and the pellet was re-suspended in 100 µL of PBS (**Figure 1**, Fraction 3). A centrifuge with a swinging bucket rotor was used for obtaining all fractions.

Preparation of samples for imaging

Unless specified, uEVs for imaging were derived from Fraction 2 shown in **Figure 1**.

To test the reproducibility of optical measurements from uEVs from urine collected at different time points, a total of four urine samples (ranging from 60 to 180 mL urine) were collected from the same healthy dog. The first urine sample was collected in the morning of the first day and the second urine sample was collected 6 hours later. Two days later, a third urine sample was collected in the morning and the fourth urine sample was collected 6 hours later.

For the uEV storage test at -20°C, uEVs were isolated immediately after collection from another healthy dog and divided into nine aliquots. Three aliquots were imaged fresh, the second group of three were imaged after 24 hours of storage, and the remaining group of three were imaged after 48 hours of storage.

The uEV samples were thawed on ice after being stored at -20°C. Before imaging, uEVs were embedded in glycerol to reduce the Brownian motion, which is the random motion of particles in a medium. Brownian motion of uEVs can cause motion artifacts during image acquisition if they are not immersed in a viscous substance [34]. This was done by heating 1 mL of 99.0% molecular biology grade glycerol (Sigma, USA) on a hotplate at 50°C for 1 min, and then placing 80 µL of warm glycerol in a 0.5 mL protein LoBind tube (Eppendorf, USA).

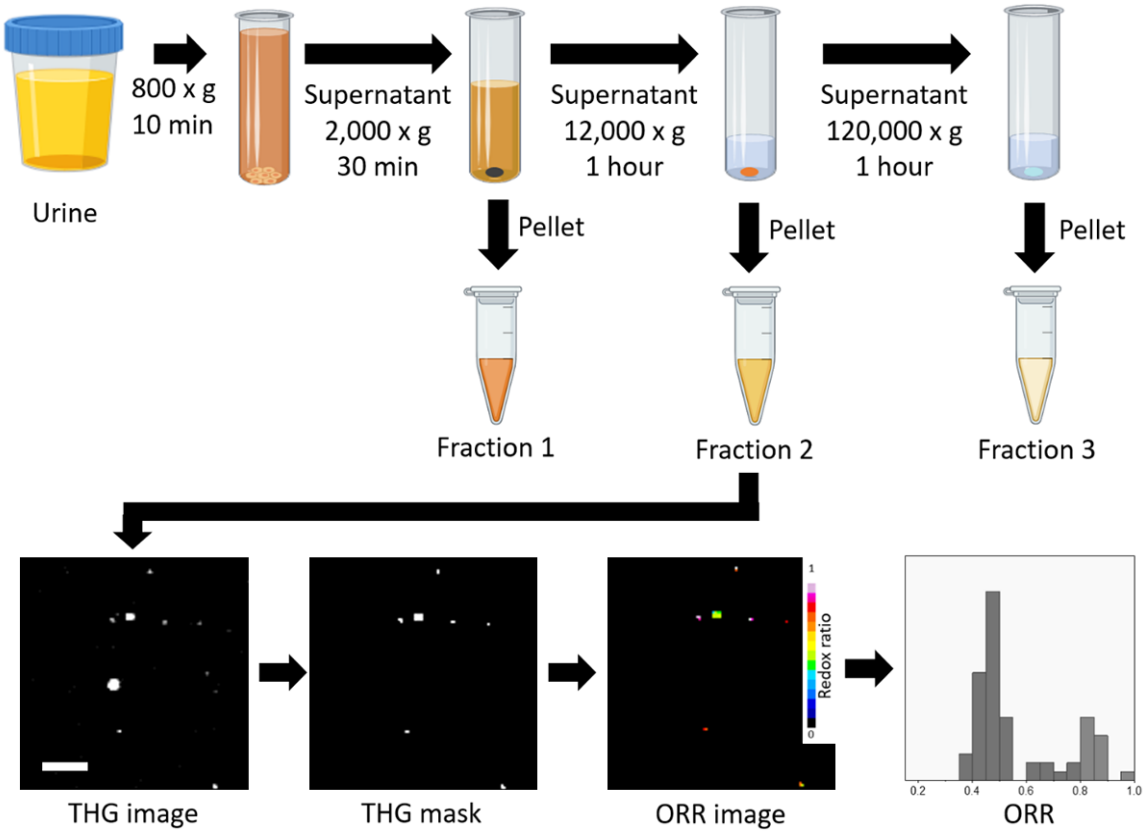

Figure 1. Scheme for uEV isolation and SLAM image analysis. Isolation method of uEVs is shown with different fractions. Image processing was done by using the THG channel for masking the 2PF and 3PF channels in order to acquire the localized autofluorescence intensities and calculate the ORRs, which can then be presented in both image and histogram formats. Scale bar = 10 μm.

Once the glycerol had cooled to approximately 18°C, 20 μL of uEV was mixed into the 80 μL of glycerol and stirred together, then transferred onto the microscope cover glass.

SLAM microscope imaging parameters

The optical imaging hardware and setup used in this study were the same as reported in our previous study [29]. Briefly, an industrial fiber laser (Satsuma, Amplitude Systemes, France) with an average power of 3.34 W was operated at a 20 MHz pulse repetition rate. The laser beam was sent into a photonic crystal fiber (PM-LMA-15, NKT Photonics, Denmark) to generate a coherent supercontinuum with high peak-power optical pulses. These supercontinuum pulses were then sent through a 640-pixel 4-f pulse shaper (MIIPS Box640, BioPhotonics Solutions Inc., USA) to select and compress the wavelength band of 1110 ± 30 nm. The average power of this band after the pulse shaper was approximately 180 mW. A galvanometer-driven mirror pair (6215H, Cambridge Technology, USA) enabled raster scanning of the beam across the imaged sample. The beam was delivered to an inverted multiphoton objective (XLPLN25XWMP2 25X, N.A. = 1.05, Olympus), which resulted in an average power of 14 mW at the sample. The microscope had a lateral resolution of ~500 nm.

Urinary EVs embedded in glycerol were placed on a coverslip above the objective lens. The imaging plane was set at 50 μm above the cover glass for all samples. The typical field-of-view of this microscope was 200 μm × 200 μm with a sampling interval of either 100 nm or 500 nm. Four sequential sets of long-pass dichroic mirrors and bandpass filters (365-375 nm filter for THG, 420-480 nm for 3PF, 540-570 nm for SHG, and 580-640 nm for 2PF) (Semrock Inc, USA) separated the collected multimodal multiphoton signals and directed them each to four photon-counting photomultiplier tubes (H7421-40, Hamamatsu, Japan). A 3-D piezoelectric stage was used for

mosaic imaging to collect image data from larger areas of the samples. A resulting field-of-view of 1 mm × 1 mm was obtained per sample by taking a 5 × 5 mosaic image. Pixel dwell time was 20 μs and the acquisition time for each 4-channel image was 8 s.

SLAM microscope detection limit

Standardized beads (NIST traceable size standards, Thermo Scientific) with sizes of 100, 200, and 500 nm were imaged using the SLAM microscope. The signal-to-noise ratio of each particle was calculated from the THG channel using the following Equation (1):

$$Signal\text{-}to\text{-}noise\ ratio = \frac{\mu_{particle}}{\sigma_{background}} \quad (1)$$

Where $\mu_{particle}$ is the mean THG intensity of the particle and $\sigma_{background}$ is the standard deviation of the THG intensity outside the particle.

Image analysis and statistical methods

MATLAB and R were used for data analysis. Masks of the imaged particles were made by thresholding the THG channel of the mosaic images (**Figure 1**). Particles larger than 2 μm were digitally removed from the image data. The number of uEVs in each image was quantified using the THG mask. Masked 2PF and 3PF signals were used for calculating the ORR of each EV using Equation (2).

$$Optical\ redox\ ratio\ (ORR) = \frac{I_{2PF}}{I_{2PF} + I_{3PF}} \approx \frac{FAD}{FAD + NAD(P)H} \quad (2)$$

The multiple measurements of the ORR, one for each individual EV, were plotted as a histogram ranging from 0 to 1. A receiver operating characteristic (ROC) curve for distinguishing bladder cancer from healthy controls was generated to determine the optimal threshold for NAD(P)H-rich EVs. The resulting cut-off for NAD(P)H-rich EVs was then selected as 0.78 to provide the best-performance of differentiating TCC of the bladder from healthy control. The Shapiro-Wilk test was used to determine normality. One-way ANOVA, Welch two-sample t-test, paired t-test, paired-sample sign test, Kruskal-Wallis test, and Kolomogorov-Smimov test were performed for statistical comparisons.

Size and concentration characterization of uEVs

The size and concentration of uEVs were determined using transmission electron microscopy (TEM), dynamic light scattering (DLS), and nanoparticle tracking analysis (NTA). TEM imaged fixed EVs with high resolution (~0.2 nm) by using an electron beam. DLS and NTA measured the size of the uEVs in solution by analyzing the scattered light from the particles. DLS was performed using the manufacturer protocol (Litesizer 500, Anton Paar). Urinary EVs were diluted to a volume of 1 mL and loaded in a disposable spectrometer cuvette for measurement. Side scatter at a 90° measurement angle with 1 min of acquisition time was performed. NTA was performed using the manufacturer protocol (NanoSight NS300, Malvern Panalytical). Settings for NTA included a syringe pump speed of 75, camera level of 13, detection threshold equal to 3, and a temperature of 21.5°C. NTA measurements were recorded 6 times with 30 seconds per track.

Results

Urinary EVs from dogs with TCC of the bladder had a higher percentage of NAD(P)H-rich EVs

Freshly isolated uEVs from dogs with TCC of the bladder and prostate cancer, as well as from healthy control dogs, were imaged using SLAM microscopy. The label-free optical signatures were then used to calculate their ORRs (**Figure 2**). **Figure 2A** shows the schematic of heterogeneous uEVs with different ORRs. **Figure 2B** is a representative ORR image of uEVs imaged by SLAM microscopy. The location and ORR of a single uEV is shown in the inset magnified image. **Figure 2C-E** are the representative ORR histograms of uEVs derived from healthy control dogs, and from dogs with TCC of the bladder and prostate cancer, respectively.

NAD(P)H-rich EVs were defined as uEVs with an ORR less than 0.78, and the relative amount (percentage) of NAD(P)H-rich uEVs in each sample was calculated. This decision threshold was selected to have a high F1-score (0.8196) for distinguishing dogs with TCC of the bladder from healthy control dogs (**Figure 3**). The area under the curve (AUC) of a ROC curve for distinguishing bladder cancer-bearing dogs from healthy control dogs was 0.8663.

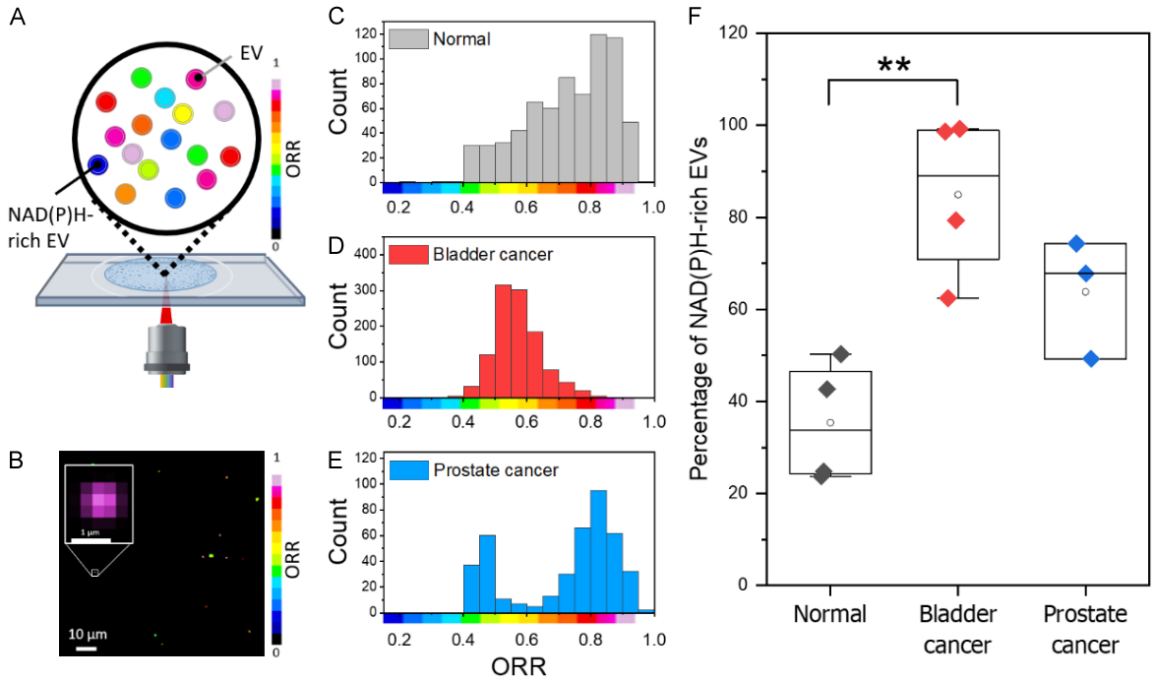

Figure 2. Comparison of ORR of uEVs derived from dogs with genitourinary cancers and healthy controls. (A) Scheme of detecting EVs with different ORRs. (B) Representative SLAM microscopy image of uEVs with pseudo-colored ORRs. Inset box is a zoomed-in image of a single uEV with ORR calculated pixel-by-pixel. Representative ORR histograms of uEVs from (C) healthy control dogs, (D) dogs with bladder cancer, and (E) dogs with prostate cancer. (F) Comparison of NADH(P)H-rich EV percentages between healthy controls and dogs with genitourinary cancers. **P ≤ 0.01.

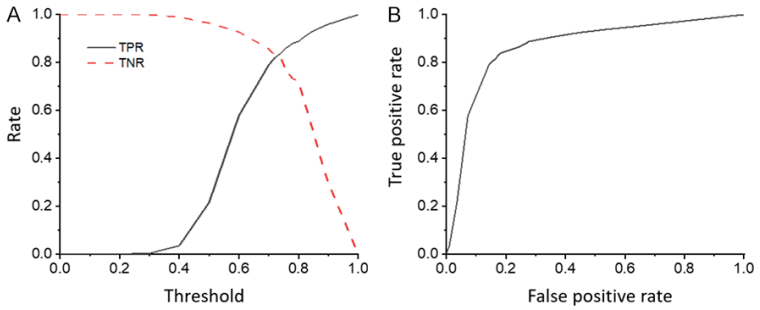

Figure 3. ROC curve analysis for determining the optimal threshold of NAD(P)H-rich EVs. (A) True positive rate (TPR) and true negative rate (TNR) per threshold for NAD(P)H-rich EVS. (B) ROC curve of sensitivity (TPR) versus specificity (false positive rate, FPR).

The mean percentage of NAD(P)H-rich uEVs from the healthy control group (number of dogs n = 4) was 35.38% while the mean percentage of NAD(P)H-rich uEVs from the groups with TCC of the bladder (n = 4) and prostate cancer (n = 3) were 84.91% and 63.80%, respectively (**Figure 2F**). The Shapiro-Wilk normality test showed that all three groups had a normal distribution (P > 0.05). Urinary EVs from dogs with TCC of the bladder had a 2.4-fold higher percentage of NAD(P)H-rich EVs compared to that of healthy control dogs. The Welch two-sample t-test showed that the four dogs in the TCC of the bladder group (mean = 0.8491, standard deviation = 0.1525) compared to the 4 dogs in the healthy control group (mean = 0.3538, standard deviation = 0.1142) had a significantly different NAD(P)H-rich EV ratio t(5.5) = 4.5, P = 0.005. A statistical power analysis with a power of 95% and an alpha level of 0.05 showed that a sample size of n = 3.3 was needed to find the difference between the control group and the TCC of the bladder group. Therefore, our sample size of n = 4 for this comparison was sufficient. The post-hoc statistical power of this study was 98.9%, and the effect size (Cohen's d) was large (g = 1.49).

Imaging and characterizing uEVs with SLAM microscopy

Sedimented pellets after the 2,000 × g, 12,000 × g, and 120,000 × g centrifugation steps

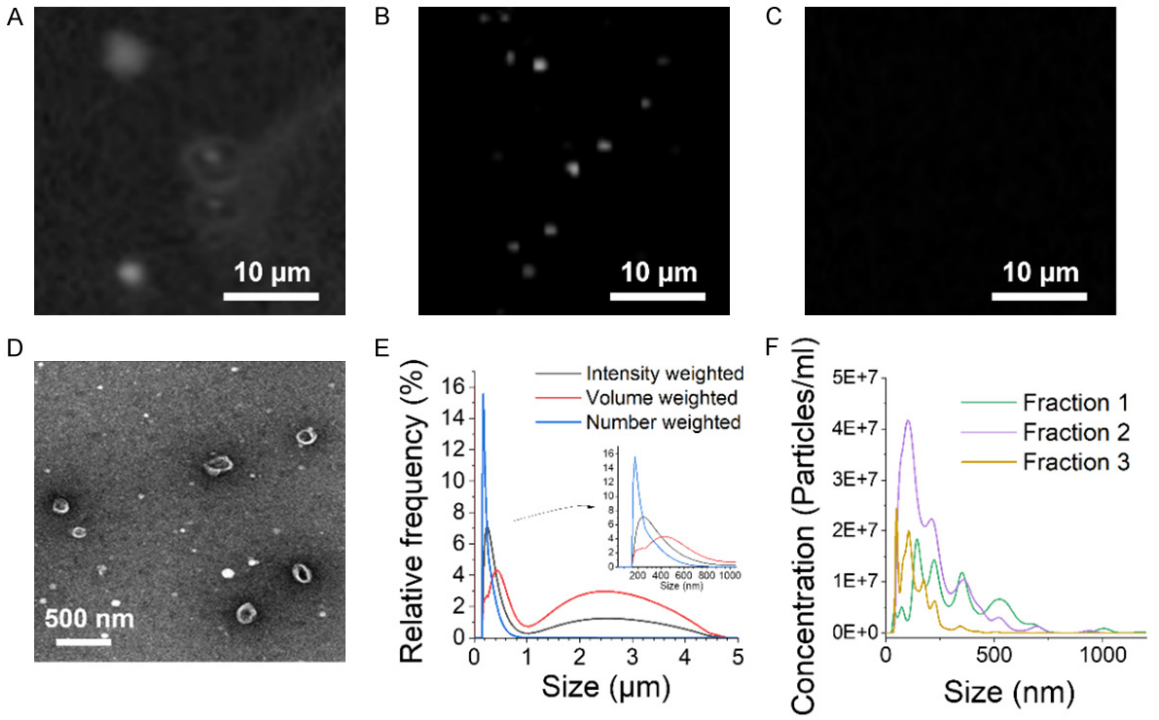

Figure 4. Characterization of uEV physical properties. Representative THG channel images of (A) Fraction 1, (B) Fraction 2 (uEVs), and (C) Fraction 3. (D) TEM image of uEVs showing a classical cup-disk shape. (E) Size distribution of uEVs analyzed by DLS. (F) Size distribution of Fraction 1 to 3 by NTA. Scales are indicated in each image.

contained: apoptotic bodies and cell debris (**Figure 1**, *Fraction 1*), large EVs also known as microvesicles (**Figure 1**, *Fraction 2*), and small EVs also referred to as exosomes (**Figure 1**, *Fraction 3*), respectively [51]. Each fraction was imaged with SLAM microscopy (**Figure 4A-C**). Fraction 2 was determined to be both pure and highly visible in SLAM microscopy, unlike Fraction 1 which showed poor purity. Fraction 3 was not visible with SLAM microscopy due to the small particle sizes and their correspondingly small volumes and small quantities of NAD(P)H.

According to the SLAM image (**Figure 4A**) and the NTA data (**Figure 4F**), Fraction 1 had particles larger than 2 μm. These large particles were likely to be cellular fragments or apoptotic bodies, which resulted in the relative impurity of particles and sizes observed in this fraction. Therefore, Fraction 1 was not used for further analysis. Particle sizes in Fraction 2 ranged from 50 nm to 2 μm and particle sizes in Fraction 3 were smaller than 200 nm (**Figure 4F**). Despite the high uniformity of particle size and concentration (> 10^9 particles/mL) of Fraction 3 particles, SLAM could not detect these very small particles (**Figure 1**, Fraction 3), which were well below the detection limit of the SLAM microscope (~200 nm) and contained an undetectably small volume of autofluorescent biomolecules. The larger EVs in Fraction 2 had both the size (> 200 nm) and concentration (> 10^8 particles/mL) suitable for SLAM imaging (**Figure 1**, Fraction 2).

A representative SLAM image of uEVs in the THG channel is shown in **Figure 4B**. The morphological characteristics of uEVs, their size and shape, were measured using TEM, DLS, and NTA. Round and cup-shaped morphologies of uEVs were observed with TEM (**Figure 4D**), confirming that the particles imaged were EVs as described and shown in previous studies [37]. The size of uEVs measured by the peak intensity of DLS was 622.6 nm and the mean size measured by TEM and NTA was 207.5 ± 48.0 nm and 209.6 ± 6.2 nm, respectively (**Figure 4D-F**). DLS factors more on highly scattering sample and due to the polydispersity of uEVs, DLS showed a larger size compared to the other methods.

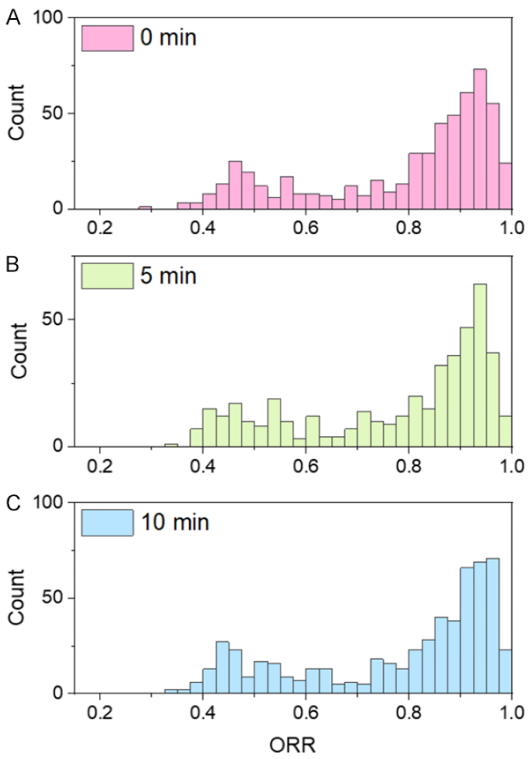

Figure 5. Reproducibility of label-free SLAM for generating histograms of the ORR from uEVs. Histograms of ORRs of uEVs are shown for measurements at (A) 0 min, (B) 5 min, (C) 10 min after the first imaging trial.

Factors affecting ORR of uEVs

Since SLAM microscopy can detect NAD(P)H and FAD autofluorescence in EVs, the ORR can be calculated using Equation (2) [29]. Reproducibility of the ORR for different conditions and factors was evaluated. First, reproducibility of the SLAM system was tested by repeatedly imaging uEV samples (n = 3) in triplicate at 5-minute intervals (**Figure 5**). The paired-sample sign test showed no significant differences between imaging sessions ($P > 0.05$).

The reproducibility of the uEV isolation procedure was tested by dividing the same urine sample into 3 vials before the isolation step. uEVs were then isolated and imaged separately. The paired-sample sign test showed no significant differences between isolation procedures ($P > 0.05$).

To test the reproducibility of the ORR from a single dog under naturally varying physiological conditions, four different time points were selected to examine the effect of urine collection time. Urine samples from a healthy dog were collected in the morning (0 hours) and afternoon (6 hours after the first collection) on the first day, and the same timed collections were conducted two days later (48 and 54 hours after the first collection). Freshly isolated uEVs were imaged with SLAM and histograms of their representative ORRs are shown in **Figure 6A-D**, where each histogram shows a distribution of values from a single collection period. The ORRs of uEVs ranged from 0.2 to 1.0. ORR histograms (n = 12) exhibited a bimodal shape with peaks at 0.54 ± 0.07 (coefficient of variation CV% = 12.2%) and 0.89 ± 0.02 (CV% = 2.5%). The percentage of NAD(P)H-enriched uEVs was not significantly different between collection times (paired t-test, $P > 0.05$) (**Figure 6E**).

The average concentration of uEVs quantified from SLAM images was 450 ± 10 particles/mm^2 and the average concentration of uEVs calculated from NTA was $4.88 \times 10^{10} \pm 1.59 \times 10^9$ particles/mL.

The effect of storing isolated uEVs on the ORR was also investigated. Isolated uEVs were stored at -20°C for 24 hours and 48 hours before imaging. ORR histograms of samples stored at -20°C are shown in **Figure 7A-C**.

The percentage of NAD(P)H-rich EVs were calculated (**Figure 7D**). After storing uEVs for 24 hours, the percentage of NAD(P)H-rich EVs decreased by 8.1%. When uEVs were stored for 48 hours, there was a significant change in the ORR distribution. Despite an apparent increase in the total number of uEVs, likely due to increased fragmentation over time, the percentage of NAD(P)H-rich EVs decreased by 31.4%, which was significantly different compared to the fresh uEVs (paired t-test, $P \leq 0.05$).

Discussion

In this study, large uEVs (microvesicles) from canine urine samples were imaged and characterized using label-free SLAM microscopy to investigate their optical signatures and the ORR as a potential biomarker for bladder cancer screening. To the best of our knowledge, this is the first study to image and characterize canine uEVs with this label-free nonlinear optical microscopy technique, opening the opportunity for using this technique to characterize uEVs in other malignancies or disease states in both canine models and in humans. In addition

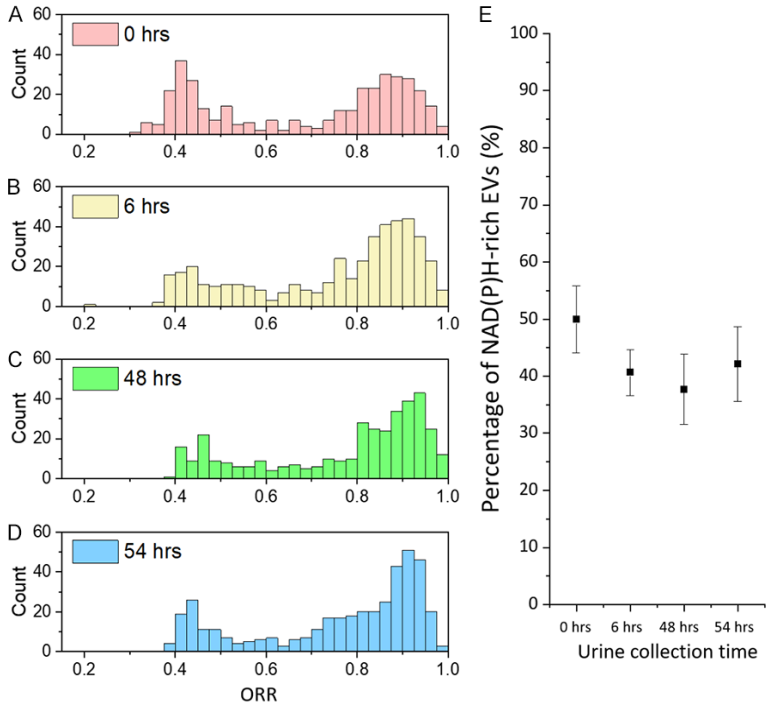

Figure 6. Effect of urine collection time on ORR (same dog, repeated sample collection to investigate intra-individual variability). ORRs of uEVs collected from (A) Day 1 morning (0 hours), (B) Day 1 afternoon (6 hours), (C) Day 3 morning (48 hours), (D) Day 3 afternoon (54 hours) from a single dog. (E) Percentage of NAD(P)H-rich EVs from the time points shown in a-d ($P > 0.05$).

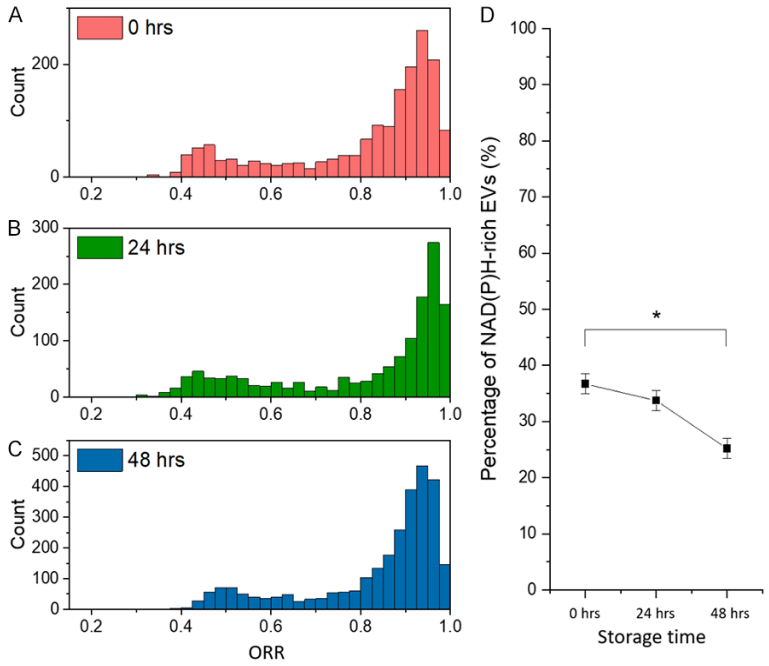

Figure 7. Effect of uEV storage on ORR. Histograms of ORRs are reported for uEVs following different storage times at -20°C. uEVs were (A) fresh (not stored), (B) stored for 24 hours, and (C) stored for 48 hours. (D) Percentage of NAD(P)H rich EVs from (A-C). *$P \leq 0.05$.

to demonstrating that it is possible to image and characterize isolated uEVs with SLAM microscopy, we found that the ORRs of uEVs could be used to differentiate uEVs from healthy dogs and dogs with TCC of the bladder.

SLAM microscopy is unique in its ability to spatially map the autofluorescence intensity of the metabolic coenzymes FAD and NAD(P)H in EVs. Multiphoton-induced autofluorescence imaging of FAD and NAD(P)H has been used to characterize the metabolic profile of various cells and tissues, specifically by calculating the ORR [29, 30]. In this study, the ORRs of single uEVs were calculated and represented in histograms for visualization and comparative analysis (**Figure 2**). The ORR distribution found in uEVs from genitourinary (bladder and prostate) cancer-bearing dogs and healthy controls were compared to examine the cancer screening potential of this method. In genitourinary cancer-bearing dogs, the mean ORR of uEVs decreased and the percentage of NAD(P)H-rich uEVs increased compared to uEVs from healthy dogs with no known history of cancer. Urinary EVs from dogs with TCC of the bladder showed a significant difference in the percentage of NAD(P)H-rich EVs compared to uEVs from healthy control dogs. Relatively higher NAD(P)H levels and lower ORRs are associated with cancer-related changes in cellular metabolism [29, 41, 52]. This suggests that higher NAD(P)H levels in cancerous cells are reflected in the uEVs that those cells pro-

duce. The collection, imaging, and characterization of uEVs with label-free SLAM microscopy therefore represents a new method to screen for metabolically-related changes that are occurring in the parent cells.

In the cases of cancer-bearing dogs, isolated uEVs contain a combination of EVs derived from both cancer cells and normal cells. Although the proportion of cancer cells may be small, cancer cells have been shown to generate significantly more EVs than normal cells [53]. Previous studies have additionally shown evidence for cancer biomarkers in uEVs [3, 14-16]. EVs indicative of increased cellular metabolic activity have a lower mean ORR and a higher percentage of NAD(P)H-rich EVs, and are hypothesized to be related to cancer cells, whereas EVs with higher ORR values are more likely from normal, non-cancerous cells [29]. The uEVs from all samples showed broad distributions of ORR values (**Figure 2C-E**). This reflects the heterogeneous nature of EVs, and the differences in cellular metabolic signatures in the EVs and their parent cells.

While uEVs from bladder cancer-bearing dogs showed a significant difference ($P \leq 0.01$) in the percentage of NAD(P)H-rich EVs compared to those from healthy controls, uEVs from prostate cancer-bearing dogs did not have a significant difference ($P > 0.05$) in the percentage of NAD(P)H-rich EVs, compared to the healthy control dogs (**Figure 2F**). This may be due to the mixed population of cancer-cell derived EVs and normal cell-derived EVs found in urine. As shown in **Figure 2E**, uEVs from prostate cancer-bearing dogs have a bimodal distribution of ORRs, likely due to the mixture of normal EVs and prostate cancer-associated EVs. The left peak of the lower ORR comes from the cancer-associated EVs and the right peak of the higher ORR comes from the normal cell-derived EVs. The percentage of NAD(P)H-rich EVs is determined by the ratio of these EV sources. In particular, two of the three prostate cancer-bearing dogs in **Figure 2F** had a high percentage (> 60%) of NAD(P)H-rich EVs, indicating increased metabolic activity related to cancer cells. These cases are likely when isolated uEV samples are rich with the prostate cancer cell-associated EVs. Whereas in one prostate cancer-bearing dog case, normal cell-associated EVs overwhelmed, resulting in a low percentage (< 60%) of NAD(P)H-rich EVs.

Unlike uEVs from the bladder (TCC in this study), which can be directly released into the urine and excreted, prostate cancer-associated uEVs must move through the prostatic ducts and into the urethra to end up in urine, or use an unknown pathway to reach the bladder [12]. Moreover, prostatic fluids are not always released into the urethra during urination. As a result, prostate cancer-associated uEVs are less likely to end up in urine, and the majority of uEVs in some prostate cancer-bearing dogs have a similar level of NAD(P)H-rich EVs as the control. In addition, prostatic adenocarcinoma and prostatic TCC arising from the prostatic urethra are difficult to distinguish, so it is possible that the small number of cases here included a mix of these two subtypes of prostate cancer in dogs. It is also likely that uEVs originating from a prostate carcinoma may pass into the blood or lymphatic circulation and then ultimately be excreted via the kidneys. For these reasons, uEVs collected from prostate cancer-bearing dogs may contain fewer cancer related uEVs compared to uEVs from bladder cancer-bearing dogs. Future work will build on previous research [54] and use SLAM microscopy to examine the relationship between prostate cancer and prostate cancer-related uEVs.

While initial results show that SLAM microscopy can be used to differentiate uEVs from healthy and bladder cancer-bearing dogs, there are several challenges and possible variations in EV studies that must be considered, such as the isolation methods and the various subpopulations of EVs, to broaden this method for screening for other types of cancer. In this study, EV isolation of the different fractions was performed using the differential ultracentrifugation method. This method was chosen because it is the most commonly used method of isolating EVs and does not require tagging. However, this method does not provide the highest purity. For example, immunoaffinity capture-based techniques filter out EVs and result in higher specificity of EV subpopulations [55]. Investigating uEVs with this method may lead to better separation of prostate cancer uEVs from the uEVs from healthy controls. However, additional filtering steps in higher-purity techniques result in lower concentrations of isolated EVs, which means the initial urine volume needed to capture enough EVs for analysis will increase. Future work will continue

to explore the effect of different isolation methods on the results obtained with SLAM microscopy and further investigate different subpopulations of EVs.

Subpopulations of EVs are generally classified by their biogenesis mechanism and/or their size [51]. While the majority of studies have focused on small EVs (exosomes), the diagnostic potential of large EVs (microvesicles) has not yet been fully explored. Previous studies showed that large EVs have similar proteins, nucleic acids, and lipid patterns as their cells of origin, and were different in composition than the small EVs [18, 19, 56]. For this reason, large EVs have potential as screening biomarkers since they carry information that can be used to make inferences about their cells of origin. While the optical resolution of SLAM microscopy was around 500 nm, the detection limit of SLAM microscopy, defined as the smallest object with a signal-to-noise ratio greater than one, was calculated to be around 200 nm using standardized polystyrene beads of various sizes. Even though the EVs were below the imaging resolution of the system, their signal could still be detected if a sufficient volume of material was present. For this reason, large EVs could be imaged while small EVs could not be detected with this imaging method. EVs showed up as a single pixel or a few pixels in the SLAM images, but with multiple signals from each of the 4 SLAM channels. This matches well with the results in **Figure 4**, which indicate that SLAM can detect large EVs, but not the small EVs from Fraction 3, which does not contain EVs larger than 200 nm. Thus, only large EVs are appropriate for label-free imaging and characterization with SLAM microscopy, given the imaging parameters of our system. However, with ongoing advances in super-resolution optical imaging techniques, future work will develop and explore the use of super-resolution SLAM microscopy for detecting the small EVs (exosomes) and compare the optical signatures between different subpopulations of EVs.

Additionally, the repeatability and robustness of using SLAM microscopy to image and characterize the ORRs of uEVs was examined by investigating different urine collections from the same dog, and by investigating the effect of storage on isolated uEV samples. In these samples, the ORR did not change significantly, regardless of the collection time of the urine, whether it was at different times during a single day, or between different days (**Figure 6**). However, the number of uEVs increased when freshly isolated uEVs were stored/frozen (**Figure 7**). These results were consistent with previous studies [55, 57]. Also, when uEVs were stored at -20°C, the mean ORR increased and the percentage of NAD(P)H-rich EVs decreased. The changing optical signatures of uEVs following storage/freezing might be related to how freezing affects EV encapsulation of NAD(P)H and FAD, or there may be metabolic changes during storage which could affect the metabolite concentrations. Previous studies have additionally examined EV storage [54, 57], yet none have used functional metrics such as the optical metabolic imaging done in this study with SLAM microscopy. In view of these initial results, it is suggested that only fresh uEVs be used for this label-free ORR characterization, largely because this method is sensitive to the quantity and autofluorescent properties of the metabolically functional biomolecules NAD(P)H and FAD. Further investigation is needed to better understand the mechanisms by which the ORRs change after uEV storage.

In summary, we demonstrated the potential of using the ORRs of uEVs as a new biomarker for bladder cancer screening. Previous studies examining the optical characteristics of EVs showed promising evidence for using EVs as a diagnostic biomarker for breast cancer [29, 40, 43]. Isolated EVs from breast cancer cell lines and breast tissues showed increased levels of NAD(P)H inside the cancer-associated EVs [29, 34, 40, 43]. Along with these previous studies of the optical characteristics of EVs in breast cancer, we are further broadening the use of label-free nonlinear optical imaging and characterization of NAD(P)H and FAD in uEVs as a screening tool of other cancers. This noninvasive approach of characterizing EVs from urine samples allows for ready clinical translation, unlike tissue imaging studies, since urine can easily and painlessly be collected with little inconvenience for human subjects. This preclinical study successfully showed evidence for using the ORR of uEVs as a screening tool for TCC of the bladder in dogs, and provided a basis for similar studies to be performed with

human subjects in the future. Although this proof-of-concept study was completed with a relatively small number of canine patients of various age, sex, and breed, it can be further advanced by controlling for more demographic variables, and by increasing both the number of patients and the types of diseases. We have investigated various factors which may change the ORR signatures of uEVs such as the storage conditions. In the future, we plan to examine additional conditions that may affect the ORR signatures, such as a urinary tract infection or inflammatory conditions. We anticipate the broader use of uEVs as a biomarker for other cancers and disease processes, since EVs are known to be generated throughout the body, and carry signatures of their parent cell of origin and any active disease process. Thus, this study provides evidence for EV-related liquid biopsy screening, and the development of label-free optical imaging and characterization tools that can aid in the screening and early detection of cancers to improve health outcomes for patients.

Acknowledgements

We thank the College of Veterinary Medicine at the University of Illinois Urbana-Champaign and Dr. Edita Aksamitiene from the Beckman Institute for supporting this research. This research was funded in part by grants from the National Institutes of Health (R01CA241618, R01CA213149). Additional information can be found at: biophotonics.illinois.edu.

Disclosure of conflict of interest

S.A.B. and S.Y. have disclosed intellectual property to the University of Illinois Urbana-Champaign and have patents associated with the use of multimodal multiphoton microscopy for imaging and characterizing extracellular vesicles. All other authors declare no conflict of interest.

Abbreviations

EV, Extracellular vesicle; uEV, Urinary extracellular vesicle; SHG, Second harmonic generation; THG, Third harmonic generation; 2PF, Two photon autofluorescence; 3PF, Three photon autofluorescence; SLAM, Simultaneous label-free autofluorescence multi-harmonic.

Address correspondence to: Stephen A Boppart, Department of Bioengineering, University of Illinois at Urbana-Champaign, IL, USA; Beckman Institute for Advanced Science and Technology, IL, USA; Carle Illinois College of Medicine, University of Illinois at Urbana-Champaign, IL, USA; Department of Electrical and Computer Engineering, University of Illinois at Urbana-Champaign, IL, USA; Cancer Center at Illinois, University of Illinois at Urbana-Champaign, IL, USA. E-mail: boppart@illinois.edu

References

[1] American Cancer Society. Cancer facts & figures 2022. Atlanta: American Cancer Society; 2021.

[2] Schubert T, Rausch S, Fahmy O, Gakis G and Stenzl A. Optical improvements in the diagnosis of bladder cancer: implications for clinical practice. Ther Adv Urol 2017; 9: 251-260.

[3] Urabe F, Kimura T, Ito K, Yamamoto Y, Tsuzuki S, Miki J, Ochiya T and Egawa S. Urinary extracellular vesicles: a rising star in bladder cancer management. Transl Androl Urol 2021; 10: 1878-1889.

[4] Daneshmand S, Patel S, Lotan Y, Pohar K, Trabulsi E, Woods M, Downs T, Huang W, Jones J, O'Donnell M, Bivalacqua T, DeCastro J, Steinberg G, Kamat A, Resnick M, Konety B, Schoenberg M, Jones JS, Bazargani S, Djaladat H, Schuckman A, Cookson M, Cross B, Stratton K, Lallas CD, Gomella L, Mann M, Johnson M, Pierorazio P, McKiernan J, Wenske S, Sankin A, Merrill M, Shabsigh A, Nielsen M, Pruthi R, Smith A, Shah JB, Taylor J and Weight C. Efficacy and safety of blue light flexible cystoscopy with hexaminolevulinate in the surveillance of bladder cancer: a phase III, comparative, multicenter study. J Urol 2018; 199: 1158-1165.

[5] Schmitz-Dräger BJ, Droller M, Lokeshwar VB, Lotan Y, Hudson MA, Van Rhijn BW, Marberger MJ, Fradet Y, Hemstreet GP, Malmstrom PU, Ogawa O, Karakiewicz PI and Shariat SF. Molecular markers for bladder cancer screening, early diagnosis, and surveillance: the WHO/ICUD consensus. Urol Int 2015; 94: 1-24.

[6] Liu YR, Ortiz-Bonilla CJ and Lee YF. Extracellular vesicles in bladder cancer: biomarkers and beyond. Int J Mol Sci 2018; 19: 2822.

[7] Doyle LM and Wang MZ. Overview of extracellular vesicles, their origin, composition, purpose, and methods for exosome isolation and analysis. Cells 2019; 8: 727.

[8] Karpman D, Ståhl AL and Arvidsson I. Extracellular vesicles in renal disease. Nat Rev Nephrol 2017; 13: 545-562.

[9] Svenningsen P, Sabaratnam R and Jensen BL. Urinary extracellular vesicles: origin, role as intercellular messengers and biomarkers; efficient sorting and potential treatment options. Acta Physiol 2020; 228.
[10] Alvarez S, Suazo C, Boltansky A, Ursu M, Carvajal D, Innocenti G, Vukusich A, Hurtado M, Villanueva S, Carreño JE, Rogelio A and Irarrazabal CE. Urinary exosomes as a source of kidney dysfunction biomarker in renal transplantation. Transplant Proc 2013; 45: 3719-3723.
[11] Raimondo F, Chinello C, Porcaro L, Magni F and Pitto M. Urinary extracellular vesicles and salt-losing tubulopathies: a proteomic approach. Proteomes 2020; 8: 9.
[12] Wang S, Kojima K, Mobley JA and West AB. Proteomic analysis of urinary extracellular vesicles reveal biomarkers for neurologic disease. EBioMedicine 2019; 45: 351-361.
[13] Zhu Q, Cheng L, Deng C, Huang L, Li J, Wang Y, Li M, Yang Q, Dong X, Su J, Lee LP and Liu F. The genetic source tracking of human urinary exosomes. Proc Natl Acad Sci 2021; 118.
[14] Royo F, Zuñiga-Garcia P, Torrano V, Loizaga A, Sanchez-Mosquera P, Ugalde-Olano A, González E, Cortazar AR, Palomo L, Fernández-Ruiz S, Lacasa-Viscasillas I, Berdasco M, Sutherland JD, Barrio R, Zabala-Letona A, Martín-Martín N, Arruabarrena-Aristorena A, Valcarcel-Jimenez L, Caro-Maldonado A, Gonzalez-Tampan J, Cachi-Fuentes G, Esteller M, Aransay AM, Unda M, Falcón-Pérez JM and Carracedo A. Transcriptomic profiling of urine extracellular vesicles reveals alterations of CDH3 in prostate cancer. Oncotarget 2016; 7: 6835-6846.
[15] Sequeiros T, Rigau M, Chiva C, Montes M, Garcia-Grau I, Garcia M, Diaz S, Celma A, Bijnsdorp I, Campos A, Di Mauro P, Borrós S, Reventós J, Doll A, Paciucci R, Pegtel M, de Torres I, Sabidó E, Morote J and Olivan M. Targeted proteomics in urinary extracellular vesicles identifies biomarkers for diagnosis and prognosis of prostate cancer. Oncotarget 2017; 8: 4960-4976.
[16] Merchant ML, Rood IM, Deegens JKJ and Klein JB. Isolation and characterization of urinary extracellular vesicles: Implications for biomarker discovery. Nat Rev Nephrol 2017; 13: 731-749.
[17] Pisitkun T, Shen RF and Knepper MA. Identification and proteomic profiling of exosomes in human urine. Proc Natl Acad Sci U S A 2004; 101: 13368-13373.
[18] Cocucci E and Meldolesi J. Ectosomes and exosomes: shedding the confusion between extracellular vesicles. Trends Cell Biol 2015; 25: 364-372.
[19] Haraszti RA, Didiot MC, Sapp E, Leszyk J, Shaffer SA, Rockwell HE, Gao F, Narain NR, DiFiglia M, Kiebish MA, Aronin N and Khvorova A. High-resolution proteomic and lipidomic analysis of exosomes and microvesicles from different cell sources. J Extracell Vesicles 2016; 5: 32570.
[20] Melo SA, Luecke LB, Kahlert C, Fernandez AF, Gammon ST, Kaye J, LeBleu VS, Mittendorf EA, Weitz J, Rahbari N, Reissfelder C, Pilarsky C, Fraga MF, Piwnica-Worms D and Kalluri R. Glypican-1 identifies cancer exosomes and detects early pancreatic cancer. Nat 2015; 523: 177-182.
[21] Bandari SK, Purushothaman A, Ramani VC, Brinkley GJ, Chandrashekar DS, Varambally S, Mobley JA, Zhang Y, Brown EE, Vlodavsky I and Sanderson RD. Chemotherapy induces secretion of exosomes loaded with heparanase that degrades extracellular matrix and impacts tumor and host cell behavior. Matrix Biol 2018; 65: 104-118.
[22] Liu W, Zhu M, Wang H, Wang W and Lu Y. Diffuse large B cell lymphoma-derived extracellular vesicles educate macrophages to promote tumours progression by increasing PGC-1β. Scand J Immunol 2020; 91: e12841.
[23] Singhto N, Vinaiphat A and Thongboonkerd V. Discrimination of urinary exosomes from microvesicles by lipidomics using thin layer liquid chromatography (TLC) coupled with MALDI-TOF mass spectrometry. Sci Reports 2019; 9: 1-11.
[24] Balbinotti H, Cadore NA, Dutra CS, DA Silva ED, Ferreira HB, Zaha A and Monteiro KM. Protein profiling of extracellular vesicles associated with cisplatin resistance in lung cancer. Anticancer Res 2020; 40: 5509-5516.
[25] Dhondt B, Van Deun J, Vermaerke S, de Marco A, Lumen N, De Wever O and Hendrix A. Urinary extracellular vesicle biomarkers in urological cancers: from discovery towards clinical implementation. Int J Biochem Cell Biol 2018; 99: 236-256.
[26] Penders J, Nagelkerke A, Cunnane EM, Pedersen SV, Pence IJ, Coombes RC and Stevens MM. Single particle automated Raman trapping analysis of breast cancer cell-derived extracellular vesicles as cancer biomarkers. ACS Nano 2021; 15: 18192-18205.
[27] Baek AE, Krawczynska N, Das Gupta A, Dvoretskiy SV, You S, Park J, Deng YH, Sorrells JE, Smith BP, Ma L, Nelson AT, McDowell HB, Sprenger A, Henn MA, Madak-Erdogan Z, Kong H, Boppart SA, Boppart MD and Nelson ER. The cholesterol metabolite 27-hydroxycholes-

terol increases the secretion of extracellular vesicles which promote breast cancer progression. Endocrinology 2021; 162: 1-18.
[28] Martinez RM, Hauser R, Liang L, Mansur A, Adir M, Dioni L, Racowsky C, Bollati V, Baccarelli AA and Machtinger R. Urinary concentrations of phenols and phthalate metabolites reflect extracellular vesicle microRNA expression in follicular fluid. Environ Int 2019; 123: 20-28.
[29] You S, Barkalifa R, Chaney EJ, Tu H, Park J, Sorrells JE, Sun Y, Liu YZ, Yang L, Chen DZ, Marjanovic M, Sinha S and Boppart SA. Label-free visualization and characterization of extracellular vesicles in breast cancer. Proc Natl Acad Sci U S A 2019; 116: 24012-24018.
[30] You S, Tu H, Chaney EJ, Sun Y, Zhao Y, Bower AJ, Liu YZ, Marjanovic M, Sinha S, Pu Y and Boppart SA. Intravital imaging by simultaneous label-free autofluorescence-multiharmonic microscopy. Nat Commun 2018; 9: 2125.
[31] Cannon TM, Shah AT and Skala MC. Autofluorescence imaging captures heterogeneous drug response differences between 2D and 3D breast cancer cultures. Biomed Opt Express 2017; 8: 1911.
[32] Walsh AJ, Cook RS, Sanders ME, Aurisicchio L, Ciliberto G, Arteaga CL and Skala MC. Quantitative optical imaging of primary tumor organoid metabolism predicts drug response in breast cancer. Cancer Res 2014; 74: 5184-5194.
[33] Chance B, Schoener B, Oshino R, Itshak F and Nakase Y. Oxidation-reduction ratio studies of mitochondria in freeze-trapped samples. NADH and flavoprotein fluorescence signals. J Biol Chem 1979; 254: 4764-4771.
[34] Sorrells JE, Martin EM, Aksamitiene E, Mukherjee P, Alex A, Chaney EJ, Marjanovic M and Boppart SA. Label-free characterization of single extracellular vesicles using two-photon fluorescence lifetime imaging microscopy of NAD(P)H. Sci Rep 2021; 11: 3308.
[35] Tominaga N, Kosaka N, Ono M, Katsuda T, Yoshioka Y, Tamura K, Lötvall J, Nakagama H and Ochiya T. Brain metastatic cancer cells release microRNA-181c-containing extracellular vesicles capable of destructing blood-brain barrier. Nat Commun 2015; 6: 1-12.
[36] Issman L, Brenner B, Talmon Y and Aharon A. Cryogenic transmission electron microscopy nanostructural study of shed microparticles. PLoS One 2013; 8: e83680.
[37] Rikkert LG, Nieuwland R, Terstappen LWMM and Coumans FAW. Quality of extracellular vesicle images by transmission electron microscopy is operator and protocol dependent. J Extracell Vesicles 2019; 8: 1555419.
[38] Duijvesz D, Versluis CY, Van Der Fels CA, Vredenbregt-Van Den Berg MS, Leivo J, Peltola MT, Bangma CH, Pettersson KS and Jenster G. Immuno-based detection of extracellular vesicles in urine as diagnostic marker for prostate cancer. Int J Cancer 2015; 137: 2869-2878.
[39] Van Der Vos KE, Abels ER, Zhang X, Lai C, Carrizosa E, Oakley D, Prabhakar S, Mardini O, Crommentuijn MH, Skog J, Krichevsky AM, Stemmer-Rachamimov A, Mempel TR, El Khoury J, Hickman SE and Breakefield XO. Directly visualized glioblastoma-derived extracellular vesicles transfer RNA to microglia/macrophages in the brain. Neuro Oncol 2016; 18: 58-69.
[40] Sun Y, You S, Tu H, Spillman DR, Chaney EJ, Marjanovic M, Li J, Barkalifa R, Wang J, Higham AM, Luckey NN, Cradock KA, Liu ZG and Boppart SA. Intraoperative visualization of the tumor microenvironment and quantification of extracellular vesicles by label-free nonlinear imaging. Sci Adv 2018; 4: eaau5603.
[41] Skala MC, Riching KM, Gendron-Fitzpatrick A, Eickhoff J, Eliceiri KW, White JG and Ramanujam N. *In vivo* multiphoton microscopy of NADH and FAD redox states, fluorescence lifetimes, and cellular morphology in precancerous epithelia. Proc Natl Acad Sci U S A 2007; 104: 19494-19499.
[42] Ostrander JH, McMahon CM, Lem S, Millon SR, Brown JQ, Seewaldt VL and Ramanujam N. Optical redox ratio differentiates breast cancer cell lines based on estrogen receptor status. Cancer Res 2010; 70: 4759-4766.
[43] Tu H, Liu Y, Marjanovic M, Chaney EJ, You S, Zhao Y and Boppart SA. Concurrence of extracellular vesicle enrichment and metabolic switch visualized label-free in the tumor microenvironment. Sci Adv 2017; 3: e1600675-e1600675.
[44] Sun Y, Chen EW, Thomas J, Liu Y, Tu H and Boppart SA. K-means clustering of coherent Raman spectra from extracellular vesicles visualized by label-free multiphoton imaging. Opt Lett 2020; 45: 3613.
[45] Knapp DW, Ramos-Vara JA, Moore GE, Dhawan D, Bonney PL and Young KE. Urinary bladder cancer in dogs, a naturally occurring model for cancer biology and drug development. ILAR J 2014; 55: 100-118.
[46] LeRoy BE and Northrup N. Prostate cancer in dogs: comparative and clinical aspects. Vet J 2009; 180: 149-162.
[47] Knapp DW, Dhawan D, Ramos-Vara JA, Ratliff TL, Cresswell GM, Utturkar S, Sommer BC, Fulkerson CM and Hahn NM. Naturally-occurring invasive urothelial carcinoma in dogs, a unique model to drive advances in managing muscle invasive bladder cancer in humans. Front Oncol 2020; 9: 1493.
[48] Cronise KE, Das S, Hernandez BG, Regan DP, Dailey DD, McGeachan RI, Lana SE, Page RL, Gustafson DL and Duval DL. Characterizing the

molecular and immune landscape of canine bladder cancer. Vet Comp Oncol 2022; 20: 69-81.

[49] Vitti Gambim V, Laufer-Amorim R, Fonseca Alves RH, Grieco V and Fonseca-Alves CE. A comparative meta-analysis and in silico analysis of differentially expressed genes and proteins in canine and human bladder cancer. Front Vet Sci 2020; 7: 891.

[50] Théry C, Amigorena S, Raposo G and Clayton A. Isolation and characterization of exosomes from cell culture supernatants and biological fluids. Curr Protoc Cell Biol 2006; 30: 3-22.

[51] Witwer KW, Buzás EI, Bemis LT, Bora A, Lässer C, Lötvall J, Nolte-'t Hoen EN, Piper MG, Sivaraman S, Skog J, Théry C, Wauben MH and Hochberg F. Standardization of sample collection, isolation and analysis methods in extracellular vesicle research. J Extracell Vesicles 2013; 2: 20360.

[52] Kolenc OI and Quinn KP. Evaluating cell metabolism through autofluorescence imaging of NAD(P)H and FAD. Antioxidants Redox Signal 2019; 30: 875-889.

[53] Liang LG, Kong MQ, Zhou S, Sheng YF, Wang P, Yu T, Inci F, Kuo WP, Li LJ, Demirci U and Wang S. An integrated double-filtration microfluidic device for isolation, enrichment and quantification of urinary extracellular vesicles for detection of bladder cancer. Sci Rep 2017; 7: 1-10.

[54] Oosthuyzen W, Sime NEL, Ivy JR, Turtle EJ, Street JM, Pound J, Bath LE, Webb DJ, Gregory CD, Bailey MA and Dear JW. Quantification of human urinary exosomes by nanoparticle tracking analysis. J Physiol 2013; 591: 5833-5842.

[55] Brett SI, Lucien F, Guo C, Williams KC, Kim Y, Durfee PN, Brinker CJ, Chin JI, Yang J and Leong HS. Immunoaffinity based methods are superior to kits for purification of prostate derived extracellular vesicles from plasma samples. Prostate 2017; 77: 1335-1343.

[56] Musante L, Bontha SV, La Salvia S, Fernandez-Piñeros A, Lannigan J, Le TH, Mas V and Erdbrügger U. Rigorous characterization of urinary extracellular vesicles (uEVs) in the low centrifugation pellet - a neglected source for uEVs. Sci Rep 2020; 10: 1-14.

[57] Erozenci LA, Pham TV, Piersma SR, Dits NFJ, Jenster GW, van Royen ME, Moorselaar RJA, Jimenez CR and Bijnsdorp IV. Simple urine storage protocol for extracellular vesicle proteomics compatible with at-home self-sampling. Sci Rep 2021; 11: 1-10.